

A finite element model with discrete embedded elements for fibre reinforced composites

Vítor M.C.F. Cunha^{a,1,*}, Joaquim A.O. Barros^{b,1}, José M. Sena-Cruz^{b,1}

^a*Department of Engineering, School of Science and Technology, University of Trás-os-Montes e Alto Douro, 5001-801 Vila Real, Portugal*

^b*Department of Civil Engineering, School of Engineering, University of Minho, 4800-058 Guimarães, Portugal*

Abstract

This work presents a numerical approach to simulate the behaviour of steel fibre reinforced concrete, FRC. The adopted strategy comprises three main steps: i) assessing the fibre pullout behaviour; ii) generation of “virtual” fibre structures and iii) modelling FRC as a two-phase material. The concrete phase is simulated with a smeared crack model, while the fibre’s positioning and orientation correspond to the fibre phase and are obtained from step ii. Finally, the fibre reinforcement mechanisms are modelled with the micro-mechanical behaviour laws obtained in step i. The agreement between the numerical and experimental results revealed the high predictive performance of the developed numerical strategy.

Keywords: FEM, Fiber reinforced concrete, Smeared crack model, Embedded discrete element

1. Introduction

2 Within steel fibre reinforced concrete, SFRC, steel fibres and matrix are
3 bonded together through a weak interface. This interface behaviour is im-
4 portant to understand and accurately model the mechanical behaviour of
5 SFRC, since the properties of this composite are greatly influenced by fi-
6 bre/matrix interface and, consequently, by the micro-mechanical fibre rein-

*Corresponding author.

Email address: vcunha@utad.pt; vcunha@civil.uminho.pt (Vítor M.C.F. Cunha)

¹ISISE – Institute for Sustainability and Innovation in Structural Engineering

7 forcement mechanisms that are mobilised during fibre pullout. For these
8 composites, when reinforced with low fibre volume ratios, the fibre contri-
9 bution benefits arise mainly, not to say almost exclusively, after the crack
10 initiation.

11 The post-cracking behaviour of random discontinuous fibre reinforced
12 brittle-matrix composites can be predicted by the use of a stress - crack
13 opening displacement relationship, $\sigma - w$. In the case of SFRC, the $\sigma - w$
14 relationship can be approximated by averaging the contributions of the indi-
15 vidual fibres bridging the matrix crack plane [1–4]. One difficulty concerning
16 the prediction of the post-cracking behaviour of SFRC in a real structure
17 is that the material behaviour in a test specimen may differ from the be-
18 haviour of a real structural element. It is well described in literature that
19 various casting procedures and structural shapes may result in predominant
20 fibre orientation into parallel planes [5, 6]. In the case of steel fibre reinforced
21 self-compacting concrete, SFRSCC, the predominant fibre orientation can be
22 along the flow itself (in the fresh state) and along the boundary surfaces due
23 to the wall effect [7–9]. The fibre orientation near the walls of a structural
24 element is not representative of the material, but of a structure [5]. A prede-
25 fined orientation of the steel fibres parallel to the tensile direction in a test
26 specimen may result in overestimating the post-cracking mechanical proper-
27 ties of SFRC, when compared with specimens with equal amount of fibres,
28 however with a random fibre orientation.

29 Having in mind this brief introduction of the principal aspects and fac-
30 tors that influence and contribute to the post-cracking behaviour of SFRC,
31 approaching SFRC as a continuum material may lead to a crude and, even,
32 incorrect estimation of the mechanical behaviour of a certain SFRC struc-
33 tural element. Even though material behaviour laws for SFRC can be ob-
34 tained with great accuracy by inverse analysis procedures of test specimens,
35 these laws may not translate the accurate material behaviour within a spe-
36 cific structural element, due to the aforementioned factors that influence the
37 behaviour of this material [10].

38 Steel fibre reinforced composites can be regarded as a two-phase material
39 made up of an unreinforced concrete matrix phase and a fibre phase. The
40 contribution of the fibre phase to the composites' post-cracking behaviour is
41 quite more important than the matrix phase. Thus, it is essential that the
42 fibre phase comprises accurate information about the fibre structure's density
43 and orientation, which depends on where and how the material is applied.
44 Adopting this approach can somehow enhance the numerical simulation of

45 SFRC structures, thus excluding the use of biased material behaviour laws,
46 e.g. laws obtained from inverse analysis procedures.

47 Therefore, based on the prior reasoning, in the present work a numeri-
48 cal approach is detailed where SFRC is treated as a heterogeneous medium
49 composed of one homogeneous phase (aggregates and paste), and another
50 one composed of the steel fibres. The fracture process of the cementitious
51 matrix (unreinforced) is modelled with a fixed smeared crack model. This
52 unreinforced concrete phase is discretised by solid finite elements. On the
53 other hand, the stress transfer between crack planes due to the reinforcing
54 mechanisms of fibres bridging active cracks is modelled with 3D embedded
55 elements. A nonlinear behaviour law is assigned to these last elements in
56 order to account for the fibre/matrix interface properties. These laws are
57 based upon the results obtained from fibre pullout tests [11]. The random
58 fibre distribution, over the matrix, is simulated with an algorithm based on
59 the Monte Carlo method, providing a realistic distribution of the fibres over
60 a bulk element. The developed algorithm takes into account factors that
61 influence the fibre structure as is the case of the so-called wall effect and
62 the high flowability of SFRSCC. The geometry, positioning and orientation
63 of the fibres are subsequently inserted in a three dimensional finite element
64 mesh. The linear elements representing the fibres are considered as embedded
65 elements. Since the stiffness of the embedded elements may not be homoge-
66 neously and isotropically distributed over the intersected "parent" elements
67 (i.e. solid elements that discretise the concrete phase), an inverse mapping
68 algorithm was developed and implemented to enable the accurate assessment
69 of the fibre's nodal forces.

70 In the past decades, several models for embedded elements have arisen
71 either for two-dimensional [12–14] and three-dimensional cases [15, 16] dif-
72 fering in their complexity, regarding either the material behaviour (full bond
73 or bond - slip capability) or geometry/positioning of the embedded elements
74 (fixed or arbitrary shape and positioning). The formulation of the embedded
75 fibre model developed in this work does not take into account fibre bond -
76 slip behaviour in a direct fashion. Within a first stage of the research, as
77 a simplification, the embedded element is modelled with a perfectly bonded
78 formulation. Hence, the bond - slip behaviour is simulated in an indirect
79 fashion from the transformation of a load - slip relationship to a tensile
80 stress - strain relation. Moreover, in the authors' knowledge this kind of ap-
81 proach is quite novel, and in the computational mechanics domain applied to
82 fibre reinforced cementitious matrices, only meso-level models using lattice

83 structures have adopted a similar philosophy, e.g. [17–19]. More recently
84 several approaches based upon the partition of unit method have arisen [20–
85 22]. Within these works, fibres are treated as discrete and are embedded in a
86 quasi-brittle matrix. However, although fibres are discrete entities in [20, 21],
87 they are not discretised into the finite element mesh regarding the composite
88 matrix. Within these models, instead of fibres being explicitly modelled, the
89 reaction forces from the fibre to the matrix are applied to the background
90 mesh at their end points. On the other hand, in the present work, the fibres
91 are explicitly modelled. In [22] a finite element model of an FRC unit cell is
92 developed in which the interface transition zones (ITZ) and the aggregates
93 were homogenised. This approach was only used for evaluating the elastic
94 properties of FRC.

95 In conclusion, the present approach treats FRC as a two phase mate-
96 rial, in which the fibres are explicitly modelled within a three-dimensional
97 background mesh (aggregates/paste). In order to avoid remeshing the vol-
98 ume finite elements for accommodating the random fibre structure, fibres are
99 modelled as embedded cables. The common embedded cable formulation is
100 only able to model the bond-slip behaviour of fibres and does not take into
101 account the dowel effect, which occurs in inclined fibres crossing an active
102 crack. For this purpose, the embedded cable formulation is extended in order
103 to include two shear components. The post-cracking behaviour of the FRC
104 is modelled having into account the fracture energy released by the matrix
105 and the bond-slip behaviour of the fibre/matrix interface.

106 2. Numerical approach

107 2.1. Concrete material model

108 The nonlinear behaviour of the concrete matrix is modelled with a fixed
109 smeared crack model. This formulation only envisages one crack per inte-
110 gration point and is a particular case of the fixed multi-directional smeared
111 crack model formulation [23–25]. The extension of this formulation for the
112 multiple crack case can be found elsewhere [26, 27]. Since a nonlinear ma-
113 terial model to simulate the crack propagation in concrete is adopted, an
114 incremental-iterative procedure is used to solve the resulting system of non-
115 linear equations. The relationship between the incremental strain and stress
116 is given by the well-known equation:

$$\Delta \underline{\sigma} = \underline{D} \Delta \underline{\varepsilon} \quad (1)$$

117 where $\Delta\sigma$ and $\Delta\varepsilon$ are, respectively, the stress and strain increment vectors
118 and \underline{D} is the tangent constitutive matrix.

119 In the adopted smeared crack model, the incremental strain vector is
120 decomposed into an incremental crack strain vector, $\Delta\varepsilon^{cr}$, and an incremen-
121 tal strain vector regarding the contribution of the uncracked concrete, i.e.
122 concrete between cracks, $\Delta\varepsilon^{co}$:

$$\Delta\varepsilon = \Delta\varepsilon^{cr} + \Delta\varepsilon^{co} \quad (2)$$

123 The strain decomposition in Eq. 2 is the main basic assumption of the
124 smeared crack models and has been widely adopted by several researchers
125 [23–28].

126 2.1.1. Crack strain and stress vectors

127 Fig. 1(a) shows a sketch of a crack plane within a solid finite element for
128 the three-dimensional case. According to the classical fracture mechanics,
129 three distinct types of crack modes can be considered (Fig. 1(b)). The crack
130 opening mode, Mode I, the in-plane shear mode, Mode II, and the out-of-
131 plane shear mode, Mode III [29, 30]. Note that, for the three-dimensional
132 case, the distinction between Mode II and III can be disregarded [29, 30],
133 see also Fig. 1(b). The referred fracture modes are correlated to the relative
134 displacements between the crack surfaces: Mode I with the crack opening
135 displacement, w , and Modes II and III with the crack sliding displacements,
136 respectively, s_1 and s_2 . The axes of the crack's local coordinate system are
137 defined by the crack normal direction, \hat{n} , and both crack tangential directions,
138 \hat{t}_1 and \hat{t}_2 , see Fig. 1(a).

139 In the smeared crack approach, w is replaced with a crack normal strain,
140 ε_n^{cr} , and both s_1 and s_2 slide components are replaced, respectively, with
141 the crack shear strain $\gamma_{t_1}^{cr}$ and $\gamma_{t_2}^{cr}$. Thus, the incremental local crack strain
142 vector, $\Delta\varepsilon_l^{cr}$, has the following components:

$$\Delta\varepsilon_l^{cr} = [\Delta\varepsilon_n^{cr}, \Delta\gamma_{t_1}^{cr}, \Delta\gamma_{t_2}^{cr}]^T \quad (3)$$

143 whereas the components of the incremental crack strain vector in the global
144 coordinate system is defined by:

$$\Delta\varepsilon^{cr} = [\Delta\varepsilon_1^{cr}, \Delta\varepsilon_2^{cr}, \Delta\varepsilon_3^{cr}, \Delta\gamma_{23}^{cr}, \Delta\gamma_{31}^{cr}, \Delta\gamma_{12}^{cr}]^T \quad (4)$$

145 The relationship between $\Delta \underline{\varepsilon}_l^{cr}$ and $\Delta \underline{\varepsilon}^{cr}$ is guaranteed by:

$$\Delta \underline{\varepsilon}^{cr} = [\underline{T}^{cr}]^T \Delta \underline{\varepsilon}_l^{cr} \quad (5)$$

146 in which \underline{T}^{cr} is the transformation matrix [27].

147 The incremental stress vector in the local coordinate system, $\Delta \underline{\sigma}_l^{cr}$, has
148 the following components:

$$\Delta \underline{\sigma}_l^{cr} = [\Delta \sigma_n^{cr}, \Delta \tau_{\hat{t}_1}^{cr}, \Delta \tau_{\hat{t}_2}^{cr}]^T \quad (6)$$

149 where $\Delta \sigma_n^{cr}$ is the incremental crack normal stress, and $\Delta \tau_{\hat{t}_1}^{cr}$ and $\Delta \tau_{\hat{t}_2}^{cr}$ are
150 the incremental crack shear stresses, respectively, in \hat{t}_1 and \hat{t}_2 directions.

151 2.1.2. Concrete constitutive law

152 An isotropic linear elastic behaviour is assumed for concrete between
153 cracks, i.e. uncracked or undamaged concrete. Thus, the constitutive relation
154 between $\Delta \underline{\varepsilon}^{co}$ and $\Delta \underline{\sigma}$ is as follows:

$$\Delta \underline{\sigma} = \underline{D}^{co} \Delta \underline{\varepsilon}^{co} \quad (7)$$

155 where \underline{D}^{co} is the well-known elastic constitutive matrix of the uncracked
156 concrete [31].

157 In similarity to Eq. 7, the crack opening and shear sliding behaviour can
158 be established in terms of a relationship between $\Delta \underline{\sigma}_l^{cr}$ and $\Delta \underline{\varepsilon}_l^{cr}$:

$$\Delta \underline{\sigma}_l^{cr} = \underline{D}^{cr} \Delta \underline{\varepsilon}_l^{cr} \quad (8)$$

159 where \underline{D}^{cr} is the crack constitutive matrix comprising Modes I, II and III
160 crack fracture parameters. Combining Eqs. 1 to 8, the constitutive law of
161 the cracked concrete is obtained [26, 28]:

$$\Delta \underline{\sigma} = \underline{D}^{crco} \Delta \underline{\varepsilon} \quad (9)$$

162 with,

$$\underline{D}^{crco} = \underline{D}^{co} - \underline{D}^{co} [\underline{T}^{cr}]^T \left(\underline{D}^{cr} + \underline{T}^{cr} \underline{D}^{co} [\underline{T}^{cr}]^T \right)^{-1} \underline{T}^{cr} \underline{D}^{co} \quad (10)$$

163 where \underline{D}^{crco} is the constitutive matrix of the cracked concrete.

164 The \underline{D}^{cr} matrix of the present model does not account for the shear-
165 normal stress coupling effect, therefore this matrix is diagonal with the non-
166 null terms being the crack's stiffness modulus associated to each fracture
167 mode (Mode I, II and III). The crack opening mode is simulated by an
168 exponential tensile-softening diagram proposed by Cornelissen *et al.* [32]
169 defined by:

$$\frac{\sigma_n^{cr}(\varepsilon_n^{cr})}{f_{ct}} = \begin{cases} \left(1 + \left(c_1 \frac{\varepsilon_n^{cr}}{\varepsilon_{n,ult}^{cr}}\right)^3\right) \exp\left(-c_2 \frac{\varepsilon_n^{cr}}{\varepsilon_{n,ult}^{cr}}\right) - \\ \frac{\varepsilon_n^{cr}}{\varepsilon_{n,ult}^{cr}} (1 + c_1^3) \exp(-c_2) & \text{if } 0 < \varepsilon_n^{cr} < \varepsilon_{n,ult}^{cr} \\ 0 & \text{if } \varepsilon_n^{cr} \geq \varepsilon_{n,ult}^{cr} \end{cases} \quad (11)$$

170 where $c_1 = 3.0$ and $c_2 = 6.93$, for plain concrete. The ultimate crack normal
171 strain, $\varepsilon_{n,ult}^{cr}$, is computed from:

$$\varepsilon_{n,ult}^{cr} = \frac{1}{k} \cdot \frac{G_f}{f_{ct} l_b} \quad (12)$$

172 where f_{ct} , G_f and l_b are the tensile strength, fracture energy and crack band
173 width, respectively, whereas k is a constant computed from:

$$k = \left[\frac{1}{c_2} \left[1 + 6 \left(\frac{c_1}{c_2} \right)^3 \right] - \left[\frac{1}{c_2} + \right. \right. \\ \left. \left. c_1^3 \left(\frac{1}{c_2} + \frac{3}{c_2^2} + \frac{6}{c_2^3} + \frac{6}{c_2^4} \right) + \frac{1}{2} (1 + c_1^3) \right] \right] \exp(-c_2) \quad (13)$$

174 The Mode I stiffness modulus, D_n^{cr} , comprised in the \underline{D}^{cr} matrix is deter-
175 mined with:

$$D_n^{cr} = f_{ct} \left[3 \left(c_1 \frac{\varepsilon_n^{cr}}{\varepsilon_{n,ult}^{cr}} \right)^2 \frac{c_1}{\varepsilon_{n,ult}^{cr}} \exp \left(-c_2 \frac{\varepsilon_n^{cr}}{\varepsilon_{n,ult}^{cr}} \right) + \right. \\ \left. \exp \left(-c_2 \frac{\varepsilon_n^{cr}}{\varepsilon_{n,ult}^{cr}} \right) \left(-c_2 \frac{\varepsilon_n^{cr}}{\varepsilon_{n,ult}^{cr}} \right) \left[1 + \left(c_1 \frac{\varepsilon_n^{cr}}{\varepsilon_{n,ult}^{cr}} \right)^3 \right] - \frac{1 + c_1^3}{\varepsilon_{n,ult}^{cr}} \exp(-c_2) \right] \quad (14)$$

176 The shear fracture modes II and III stiffness modulus, respectively, D_{t1}^{cr}
177 and D_{t2}^{cr} , are computed from:

$$D_{t1}^{cr} = D_{t2}^{cr} = \frac{\beta}{1 - \beta} G_c \quad (15)$$

178 where G_c and β are, respectively, the elastic shear modulus and the shear
179 retention factor. A linear softening constitutive law is used to model the shear
180 degradation of the concrete with the increase of the crack normal strain:

$$\beta = 1 - \frac{\varepsilon_n^{cr}}{\varepsilon_{n,ult}^{cr}} \quad (16)$$

181 2.2. Fibre structure modelling

182 In the present approach, the fibre structure that represents, with a certain
183 level of accuracy, the distribution of fibres in a hardened matrix is randomly
184 generated by a Monte Carlo procedure. The algorithm to generate the fibres'
185 positioning and orientation as well as its performance can be found elsewhere
186 [10]. After the generation of the element mesh representing the fibres, there
187 is the need to insert this "fibre mesh" into the solid three-dimensional mesh
188 that models the plain concrete.

189 In the present work, since it is assumed that the embedded elements (rep-
190 resenting the fibres) are always straight, it is enough to represent the fibre by
191 two end-nodes defined in the global coordinate system. It should be noted,
192 however, that a fibre can intersect one or even several solid elements, thus
193 there is the need to allow for several additional points for the distinct inter-
194 section points. Therefore, a fibre can be represented by several embedded
195 elements, in which each element contributes exclusively to the reinforcement

196 of a single solid element (brick). The determination of the coordinates of
197 these intersecting points was performed by an inverse mapping technique.
198 The search of the intersecting points was carried out at the embedded ele-
199 ment's natural axis.

200 2.2.1. Inverse mapping technique

201 The inverse mapping technique basically consists in looking within the
202 solid element's natural coordinate domain (ξ, η, ς) , correspondent to the
203 solid global coordinates, (x_1^c, x_2^c, x_3^c) , which match the embedded element's
204 global coordinates, i.e $(x_1^f, x_2^f, x_3^f) \equiv (x_1^c, x_2^c, x_3^c)$, see Fig. 2.

$$\begin{bmatrix} \sum_{i=1}^{n_f} N_i^f(\zeta) x_{1,i}^f \\ \sum_{i=1}^{n_f} N_i^f(\zeta) x_{2,i}^f \\ \sum_{i=1}^{n_f} N_i^f(\zeta) x_{3,i}^f \end{bmatrix} - \begin{bmatrix} \sum_{i=1}^{n_c} N_i^c(\xi, \eta, \varsigma) x_{1,i}^c \\ \sum_{i=1}^{n_c} N_i^c(\xi, \eta, \varsigma) x_{2,i}^c \\ \sum_{i=1}^{n_c} N_i^c(\xi, \eta, \varsigma) x_{3,i}^c \end{bmatrix} = 0 \quad (17)$$

205 In order to obtain the embedded element's point $P(x_{1,p}, x_{2,p}, x_{3,p})$ that in-
206 tersects the solid element, Eq. 17 is solved by the Newton-Raphson method.
207 Whenever this method fails to converge the bisection method is used. There-
208 fore, for each embedded element, a search is performed within the natural
209 coordinate system (ζ) . The embedded element's point ζ_p , which intercepts,
210 skirts or touches one of the solid element's faces (Fig. 2), must comply with
211 one of the following conditions:

$$\begin{aligned} \|\xi^f\| = 1 \wedge \|\eta^f\| \leq 1 \wedge \|\varsigma^f\| \leq 1 \\ \|\xi^f\| \leq 1 \wedge \|\eta^f\| = 1 \wedge \|\varsigma^f\| \leq 1 \\ \|\xi^f\| \leq 1 \wedge \|\eta^f\| \leq 1 \wedge \|\varsigma^f\| = 1 \end{aligned} \quad (18)$$

212 where ξ^f , η^f and ς^f are the embedded element's natural coordinates within
213 the solid element's natural coordinate system.

214 After the completion of the point P determination, the embedded ele-
215 ments' mesh data is rewritten in order to take into account the compatibility
216 between the embedded fibres and the solid mesh elements. Coincident nodes

217 from different solid element faces belonging to the same embedded element
218 are merged, and finally the embedded elements' nodes are renumbered.

219 2.2.2. Constitutive model for the embedded fibres

220 As already mentioned, the present formulation of the embedded fibre
221 model does not take into account fibre bond - slip behaviour in a direct fash-
222 ion. Therefore, the embedded element is modelled with a perfectly bonded
223 assumption. In fact, the bond - slip behaviour is simulated in an indirect
224 fashion from the transformation of a load - slip relationship, $P - s$, to a
225 tensile stress - strain relation, $\sigma_f - \varepsilon_f$.

226 The constitutive laws for the embedded fibres were determined from fibre
227 pullout tests carried out in the scope of the present research project [10].
228 Three distinct $\sigma_f - \varepsilon_f$ laws corresponding, respectively, to the pullout in-
229 clination angles of the studied fibres, α , (0° , 30° and 60°) were ascertained
230 [10]. Fig. 3 depicts the procedure adopted to obtain the $\sigma_f - \varepsilon_f$ relationship,
231 where ε_f , l_b and s are, respectively, the embedded fibre strain, the crack band
232 width and the steel fibre's slip; σ_f is the ratio between the pullout force, P ,
233 and the fibre's cross-sectional area, A_f .

234 The trilinear $\sigma_f - \varepsilon_f$ diagram used to model the fibres including the bond
235 - slip effect was obtained by fitting the experimental pullout load-slip curves.
236 For each fibre inclination angle, α , an average pullout load-slip curve was
237 computed from the experimental envelope of the series with an embedded
238 length of 10 mm and 20 mm, thus corresponding, approximately, to the
239 expected pullout load-slip behaviour of a fibre with an embedded length of
240 15 mm. This averaging procedure was adopted for two reasons. The influence
241 of the fibre embedded length on the pullout behaviour is not so significant as
242 the fibre inclination effect, and its influence is almost linear [10]. In addition,
243 the theoretical average value of the embedded length of a fibre crossing an
244 active crack is $l_f/4 = 15$ mm [33], where l_f is the fibre length (end-to-end).
245 This simplification has a rational and scientific basis. Additionally, in the
246 developed model only the most relevant data obtained from fibre pullout
247 tests is included in the model, thus optimising the computation time.

248 The tensile stress - strain law assigned to an embedded fibre depends
249 on the inclination angle, θ , between the fibre and the vector normal to the
250 active crack surface, see Fig. 4. Moreover, the $\sigma_f - \varepsilon_f$ also depends on the
251 crack band width, l_b , of the intersected solid element, see Fig. 3. Due to the
252 impossibility of having a $\sigma_f - \varepsilon_f$ law for every possible inclination angle and
253 embedded length, the $\sigma_f - \varepsilon_f$ laws obtained from the pullout tests with an

254 angle, α , of 0° , 30° and 60° were assigned to the embedded fibres with an
255 orientation towards the active crack surface θ ranging from, respectively, $[0^\circ$,
256 $15^\circ[$, $[15^\circ$, $45^\circ[$ and $[45^\circ$, $75^\circ[$. The contribution of the fibres with θ in the
257 interval $[75^\circ$, $90^\circ]$ was neglected.

258 2.2.3. Evaluation of the stiffness matrix of the concrete and embedded fibre 259 structure

260 The element stiffness matrix representing a concrete bulk reinforced with
261 fibres can be expressed as:

$$\underline{K}^{rc} = \underline{K}^{crco} + \sum_{i=1}^{n_f} \underline{K}_i^f \quad (19)$$

262 where \underline{K}^{crco} , \underline{K}_i^f and n_f are, respectively, the concrete element stiffness ma-
263 trix, the stiffness matrix of the i^{th} fibre that is embodied into the concrete
264 mother-element, and the total number of embodied fibres in the concrete
265 element. The concrete element stiffness matrix is given by:

$$\underline{K}^{crco} = \int_V \underline{B}^T \underline{D}^{crco} \underline{B} dV \quad (20)$$

266 where \underline{D}^{crco} is the cracked concrete's constitutive matrix (determined from
267 Eq. 10) and \underline{B} is the well-known strain - displacement matrix of a solid
268 element [31].

269 The axial contribution of the fibre reinforcement to the stiffness matrix
270 can be computed by the internal work regarding the axial component as
271 follows:

$$\begin{aligned} W_a &= \int_V \delta \varepsilon_f^T \sigma_f dV \\ &= \int_L \delta \varepsilon_f^T E_f \varepsilon_f A_f dL \end{aligned} \quad (21)$$

272 with,

$$dL = \sqrt{\left(\frac{dx_1}{ds}\right)^2 + \left(\frac{dx_2}{ds}\right)^2 + \left(\frac{dx_3}{ds}\right)^2} \cdot ds = J ds \quad (22)$$

273 where σ_f , ε_f and A_f are the stress, the strain and the cross-sectional area of
274 the fibre, whereas J is the Jacobian at the sampling point of the integration
275 scheme adopted in the numerical evaluation of the \underline{K}_i^f . Thus, substituting
276 Eq. 22 in Eq. 21, the internal work can be computed in natural coordinates
277 by:

$$W_a = \int_{-1}^{+1} \delta \varepsilon_f^T E_f \varepsilon_f A_f J ds \quad (23)$$

278 The stiffness matrix is obtained by substituting $\varepsilon_f = \underline{T}_1^f \underline{B} \underline{d}$ in Eq. 23, where
279 \underline{d} is the vector with the solid element's nodal displacements and \underline{T}_1^f is the
280 vector corresponding to the first line of the transformation matrix from the
281 fibre's local coordinate system to the global coordinate system, \underline{T}^f , given by:

$$\underline{T}^f = \begin{bmatrix} a_{11}^2 & a_{12}^2 & a_{13}^2 & a_{12} a_{13} & \dots \\ a_{21} a_{31} & a_{22} a_{32} & a_{23} a_{33} & 0.5(a_{22} a_{33} + a_{23} a_{32}) & \dots \\ a_{11} a_{31} & a_{12} a_{32} & a_{13} a_{33} & 0.5(a_{13} a_{32} + a_{12} a_{33}) & \dots \\ \dots & a_{11} a_{13} & a_{11} a_{12} & \dots & \dots \\ \dots & 0.5(a_{23} a_{31} + a_{21} a_{33}) & 0.5(a_{21} a_{32} + a_{12} a_{31}) & \dots & \dots \\ \dots & 0.5(a_{13} a_{31} + a_{11} a_{33}) & 0.5(a_{12} a_{31} + a_{11} a_{32}) & \dots & \dots \end{bmatrix} \quad (24)$$

282 where a_{ij} are the components of the matrix \underline{a} comprising the direction cosines,
283 i.e. the projection of the fibre's local coordinate system (x'_1, x'_2, x'_3) versors
284 towards the global coordinate system (x_1, x_2, x_3) versors (see Fig. 4):

$$\underline{a}^f = \begin{bmatrix} a_{11} & a_{12} & a_{13} \\ a_{21} & a_{22} & a_{23} \\ a_{31} & a_{32} & a_{33} \end{bmatrix} = \begin{bmatrix} \cos(x'_1, x_1) & \cos(x'_1, x_2) & \cos(x'_1, x_3) \\ \cos(x'_2, x_1) & \cos(x'_2, x_2) & \cos(x'_2, x_3) \\ \cos(x'_3, x_1) & \cos(x'_3, x_2) & \cos(x'_3, x_3) \end{bmatrix} \quad (25)$$

285 Hence, the component of the stiffness matrix with the fibre's axial contribu-
286 tion is given by:

$$\underline{K}_a^f = \int_{-1}^1 \underline{B}^T \left[\underline{T}_1^f \right]^T \underline{T}_1^f \underline{B} E_f A_f J ds \quad (26)$$

287 In a similar way, the components of the fibre stiffness matrix with the shear
288 contribution is given by:

$$\begin{aligned}
K_{s,1}^f &= \int_{-1}^1 \underline{B}^T \left[\underline{T}_2^f \right]^T \underline{T}_2^f \underline{B} G \bar{A}_f J ds \\
K_{s,2}^f &= \int_{-1}^1 \underline{B}^T \left[\underline{T}_3^f \right]^T \underline{T}_3^f \underline{B} G \bar{A}_f J ds
\end{aligned} \tag{27}$$

289 where G is the fibre's elastic shear modulus, and \underline{T}_2^f and \underline{T}_3^f are, respectively,
290 the vector corresponding to the second and third lines of the transformation
291 matrix, see Eq. 24. For the shear components, the value adopted for \bar{A}_f is
292 the reduced shear area for circular sections [34].

293 The equivalent nodal forces vector, \underline{q}^e , is computed from:

$$\underline{q}^e = \underbrace{\int_V \underline{B}^T \underline{\sigma} dV}_{\text{concrete}} + \underbrace{\int_{-1}^1 \underline{B}^T \underline{T}^T \sigma_f A_f J ds}_{\text{axial component}} + \underbrace{\int_{-1}^1 \underline{B}^T \underline{T}^T \underline{\tau}_f \bar{A}_f J ds}_{\text{shear components}} \tag{28}$$

fibre contribution

294 where σ_f is the fibre stress with axial component obtained from the adopted
295 tensile stress - strain diagram for modelling the fibre pullout behaviour. On
296 the other hand, $\underline{\tau}_f$ is the fibre's stress vector with the two shear components.
297 For the fibre shear behaviour an elasto-plastic behaviour was adopted. A
298 shear stress cut-off was introduced for shear strains higher than 0.01. More-
299 over, the fibre's shear contribution was only taken into account for crack
300 opening width, w , smaller than 0.5 mm ($w = \varepsilon_n^c l_b$). The shear stress yield
301 criterion used in the present work is assumed to be independent from the
302 axial stress.

303 3. Numerical simulations

304 The model performance is appraised by simulating uniaxial tensile tests
305 and three-point bending tests carried out with self-compacting concrete spec-
306 imens reinforced with 30 and 45 kg/m³ steel fibres, designated as Cf30 and
307 Cf45 series, respectively. Details about the tests set-up and specimens geom-
308 etry can be found elsewhere [10, 35, 36]. The experimental results obtained
309 in both uniaxial and bending tests for the studied fibre contents were mod-
310 elled with two numerical curves. These numerical curves were attained by

311 running under the FEM basis two distinct "virtual" fibre structures obtained
 312 from the procedure described in section 2.2. The two numerical simulations
 313 obtained per series were distinguished and designated, respectively, as curve
 314 A and B. Although curves A and B have distinct fibre structures, within each
 315 series/specimens both have exactly the same volumetric fibre content and,
 316 consequently, the same total number of fibres within the specimen's volume.
 317 However, note that the arrangement of the fibres within the concrete mesh
 318 is distinct for curves A and B. Due to the randomness implicit to the devel-
 319 oped approach there is the possibility of obtaining an envelope of numerical
 320 responses, i.e. with a certain scatter associated to distinct fibre structures,
 321 as a consequence of distinct number of fibres crossing an active crack and
 322 with distinct inclination angles.

323 Table 3 includes both the number of fibres that intersect the active crack
 324 surface and the correspondent orientation factor, η , regarding both curves A
 325 and B for each test and series modelled. Note that the orientation factor of
 326 the fibres crossing the crack surface was computed as:

$$\eta = \sum_{i=1}^{N_f} \cos(\theta_i) / N_f \quad (29)$$

327 where N_f is the total number of fibres that intersect the crack plane and
 328 $\cos(\theta_i)$ is the scalar product of the i^{th} fibre versor (which also intersects the
 329 crack plane) and the versor normal to the crack plane, and θ_i is the out-plane
 330 angle.

331 3.1. Uniaxial tensile tests

332 Fig. 5(a) represents the mesh used exclusively for the concrete matrix
 333 phase, whereas Figs. 5(b) and 5(c) depict three-dimensional meshes used for
 334 modelling the steel fibre contribution, for the Cf30 and Cf45 series, respec-
 335 tively. Note that the fibres intersected by the notch were not included into
 336 the finite element mesh. Moreover, since the numerical fibre mesh was ob-
 337 tained for a cylinder with 300 mm of height, and on the other hand the tested
 338 cylinder had a height of only 150 mm, the fibres that are not fully contained
 339 in only one half of the specimen were also removed. These simplifications
 340 have almost no influence on the numerical simulations, since the fibre con-
 341 tribution outside the fracture zone is very reduced for the tensile behaviour
 342 of this type of specimen.

343 In the present mesh Lagrangian 8-node solid elements are used for mod-
344 elling the plain concrete contribution. Since the specimen has a notch at its
345 mid-height, all the nonlinear behaviour is localised at the notch region, thus
346 a $2 \times 2 \times 1$ Gauss-Legendre integration scheme is used (1 integration point
347 in the loading direction). The remaining solid elements are modelled with
348 linear elastic behaviour, and a $2 \times 2 \times 2$ Gauss-Legendre integration scheme
349 is adopted. The Cornelissen *et al.* [32] softening law was used for modelling
350 the post-cracking nonlinear behaviour of SCC. The material properties of
351 the concrete matrix used in the simulations are included in Table 1. These
352 values were obtained by taking into account the strength class [37] regis-
353 tered for the Cf30 and Cf45 series. On the other hand, the steel fibres are
354 modelled with 3D embedded elements with two integration points (Gauss-
355 Legendre). Nonlinear behaviour is ascribed to all the embedded elements.
356 Nevertheless, only the embedded elements belonging to a “mother” element
357 (brick) with nonlinear behaviour, i.e. cracking, develop nonlinear behaviour,
358 i.e. fibre pullout. The other embedded elements remain in the elastic phase.
359 Table 2 includes the parameters of the tri-linear $\sigma_f - \varepsilon_f$ laws ascribed to the
360 embedded elements.

361 Figs. 6 and 7 depict the numerical simulations of the uniaxial tensile tests
362 of the Cf30 and Cf45 series, respectively. A good agreement with the exper-
363 imental responses was obtained for both series. The predicted numerical
364 tensile strength is near the upper bound limit of the experimental envelope.
365 This is feasible, because during testing it is almost impossible to completely
366 exclude eccentricities, thus a slight misalignment of the specimen with the
367 loading axis will introduce a bending moment. Due to this moment, the ex-
368 perimental tensile strength is smaller than the correspondent numerical one.
369 Moreover, the maximum tensile stress obtained in the numerical simulations,
370 i.e. maximum load divided per fractured area, is smaller than the value of
371 the tensile strength used in the local material law for concrete (see Table 1).
372 This is due to the stress concentrations that arise at the notch tip. Thus,
373 when the concrete’s tensile strength is attained near the notch tip, for the
374 maximum load capacity of the specimen, the overall tensile stress computed
375 from averaging the tensile load with the net cross section at the notch will be
376 smaller than the concrete’s tensile strength defined as a material property.

377 After the coalescence of micro-cracking into a macro-crack, the tensile
378 stress drops abruptly to a crack opening width varying from, approximately,
379 0.08 to 0.16 mm. Above this crack width level, the reinforcement mechanisms
380 of the hooked steel fibres start to be mobilised, enabling a slight hardening

381 of the tensile response. Figs. 8(a) and 8(b) show the fibres intersecting the
382 crack plane regarding the fibre structures used to obtain the numerical curve
383 A for the Cf30 and Cf45 series, respectively. Figs. 8(c) and 8(d) depict the
384 normal stresses at the crack plane for a crack opening width of 0.16 mm for
385 the curve A of the Cf30 and Cf45 series, respectively. Due to the higher
386 number of fibres intersecting the crack plane a higher stress transfer level for
387 the Cf45 series is clearly visible, which is translated into an overall tensile
388 stress of nearly 1.2 MPa in opposition to the 0.8 MPa observed for the Cf30
389 series (see curves A in Figs. 6 and 7).

390 The differences observed in the residual tensile strengths between the
391 Cf30 and Cf45 series are more considerable for higher crack opening widths,
392 mainly for $w > 1$ mm (Figs. 6 and 7). These differences in the post-cracking
393 behaviour are not just ascribed to the higher number of fibres intersecting the
394 crack plane in the Cf45 series, as a direct consequence of the higher volumetric
395 fibre content. The full explanation and discussion of this phenomenon
396 is out of the scope of the present work and can be found elsewhere [10].
397 Nevertheless, and very briefly, it can be pointed out that those differences
398 in the post-cracking behaviour can be ascribed to distinct micro-mechanical
399 behaviours of the fibres in the Cf30 and C45 series. For the Cf45 series,
400 fibre rupture did not occur so often due to both a less resistant matrix and
401 the reduction of the average fibre orientation angle towards the crack plane
402 [10]. Figs. 8(e) and 8(f) depict the normal stresses at the crack plane for a
403 crack opening width of 2 mm for the Cf30 and Cf45 series, respectively. The
404 differences in the grade of the residual crack stresses between Cf30 and Cf45
405 is quite notorious.

406 3.2. Three-point bending tests

407 The sketch of the finite element mesh used to model the concrete matrix
408 phase in the prismatic specimens for both Cf30 and Cf45 series is included
409 in Fig. 9(a). On the other hand, Fig. 9(b) provides a three-dimensional view
410 of one mesh used to model the steel fibre phase contribution for the Cf30
411 series. The steel fibre mesh for the Cf45 series is not represented here since
412 its graphical rendering would not enable a clear visualisation. The fibres
413 intersected by the notch were removed, as was performed for the tensile test
414 simulations.

415 Lagrangian 8-node solid elements are also used to model the concrete
416 behaviour in the prismatic specimen. In similarity to what was carried out
417 for modelling the tensile tests, all the nonlinear behaviour was localised at

418 the notch region (at mid-span of the beam). Thus, a $2 \times 1 \times 2$ Gauss-Legendre
419 integration scheme is used (1 integration point in the normal direction to the
420 crack surface, i.e. in the longitudinal axis of the prism). The remaining solid
421 elements are assumed to have a linear elastic behaviour, and a $2 \times 2 \times 2$
422 Gauss-Legendre integration scheme is adopted. The Cornelissen *et al.* [32]
423 softening law was used to simulate the SCC fracture mode I propagation.
424 The values of the material properties of the concrete used in the current
425 simulations are the same already adopted in the simulations of the uniaxial
426 tensile tests, see Table 1. The steel fibres are modelled with 3D embedded
427 elements with two Gauss-Legendre integration points. Only the embedded
428 elements, which intersect a crack at the integration point of the solid element,
429 develop nonlinear behaviour.

430 The numerical simulations of the three-point bending tests are included
431 in Figs. 10(a) and 10(b) for the Cf30 and Cf45 series, respectively. The
432 agreement between the numerical curve and the experimental results was
433 quite good for both series.

434 Regarding the Cf30 series, the load at crack initiation obtained in the
435 numerical simulation was modelled with accuracy. However, for the numer-
436 ical curve B a significant load decay is observed down to the lower bound,
437 L.B., of the envelope of the experimental results. Up to a deflection of nearly
438 0.75 mm, the numerical curve B arises just below the L.B. of the experimen-
439 tal envelope. After the later deflection, the curve is within the experimental
440 envelope. On the other hand, the numerical curve A (with a higher number
441 of fibres intersecting the crack plane, see Table 3) was always within the ex-
442 perimental envelope, thus the aforementioned decay was not observed. The
443 agreement between the numerical curves of the Cf45 series and the experi-
444 mental results was also high. Moreover, the abovementioned load decay was
445 also not observed for neither of the numerical simulations of the Cf45 series.

446 4. Conclusions

447 In this work a numerical approach to model the behaviour of steel fibre
448 reinforced concrete, SFRC, was presented based upon the micro-mechanical
449 behaviour of the steel fibres. The adopted strategy comprises three main
450 steps: i) assessing the fibre pullout behaviour (micro-level); ii) generation of
451 "virtual" fibre structures (meso-level); and iii) modelling the SFRSCC as a
452 two phase material, in which the concrete phase is modelled with a smeared
453 crack model, while the positioning and orientation of the fibres correspond to

454 the fibre phase and are obtained from step ii. Finally, the fibre reinforcement
455 mechanisms are modelled with the micro-mechanical behaviour laws obtained
456 in step i.

457 The numerical finite element simulations of both the uniaxial tensile tests
458 and three-point bending tests revealed a very good agreement with the ex-
459 perimental test results. Having a realistic approximation of the actual fibre
460 distribution and with the knowledge of the micro-mechanical behaviour of
461 the fibres, it is possible to predict the macro-mechanical behaviour of SFRC
462 specimens. Moreover, since for the generation of the "virtual" fibre struc-
463 tures a Monte-Carlo procedure was adopted due to the randomness implicit
464 to this approach there is the possibility of obtaining an envelope of numerical
465 responses. The scatter of the numerical simulations is ascribed to the distinct
466 fibre structures as a consequence of a different number of fibres crossing an
467 active crack and with distinct inclination angles, which will be mobilised in
468 distinct levels, thus contributing in different ways to the overall mechanical
469 behaviour. This approach was only used for modelling notched specimens,
470 i.e. where the fracture plane is previously known. In a future stage, further
471 numerical research should be extended to specimens with other geometries
472 and loading conditions.

473 5. Acknowledgements

474 The authors of the present work wish to acknowledge the support provided
475 by ADI "FEDER - Programa Operacional Factores de Competetividade"
476 research project QREN, N. 5387, LEGOUSE.

477 References

- 478 [1] K. Visalvanich, A. E. Naaman, Fracture model for fiber reinforced con-
479 crete, ACI J. 80 (2) (1983) 128–138.
- 480 [2] V. C. Li, Y. Wang, S. Baker, A micromechanical model of tension soft-
481 ening and bridging toughening of short random fiber reinforced brittle
482 matrix composites, J. Mech. Phys. Solids 39 (5) (1991) 607–625.
- 483 [3] V. C. Li, Postcrack scaling relations for fiber reinforced cementitious
484 composites, ASCE J. Mater. Civil Eng. 4 (1) (1992) 41–57.

- 485 [4] M. Maalej, V. C. Li, T. Hashida, Effect of fiber rupture on tensile prop-
486 erties of short fiber composites, *J. Eng. Mech.-ASCE* 121 (8) (1995)
487 903–913.
- 488 [5] P. Stroeven, Stereology of concrete reinforced with short steel fibres,
489 *Fract. Mech. Struct. Aspects Concr.* 31 (1986) 15–28.
- 490 [6] RILEM TC 162-TDF, Test and design methods for steel fibre reinforced
491 concrete – design of steel fibre reinforced concrete using the σ -w method:
492 principles and application, *Mater. Struct.* 35 (249) (2002) 262–276.
- 493 [7] S. Grünewald, J. C. Walraven, Self-compacting fibre reinforced concrete
494 - orientation effect of steel fibres in large beams, in: *Workshop - Design*
495 *rules for steel fibre reinforced concrete structures*, Oslo, Norway, 2003,
496 pp. 107–113.
- 497 [8] P. Stähli, R. Custer, J. van Mier, On flow properties, fibre distribution,
498 fibre orientation and flexural behaviour of FRC, *Mater. Struct.* 41 (1)
499 (2008) 189–196.
- 500 [9] L. Vandewalle, G. Heirman, F. Van Rickstal, Fibre orientation in self-
501 comapcting fibre reinforced concrete, in: R. Gettu (Ed.), *Sevnth. Intl.*
502 *RILEM Symposium on Fibre Reinforced Concrete: Design and Appli-*
503 *cations*, Chennai, India, 2008, pp. 719–728.
- 504 [10] V. M. C. F. Cunha, Steel fibre reinforced self-compacting con-
505 crete – from micromechanics to composite behaviour, Ph.D. the-
506 sis, Dep. Civil Engineering, University of Minho, Portugal (2010),
507 (<http://hdl.handle.net/1822/10667>).
- 508 [11] V. M. C. F. Cunha, J. A. O. Barros, J. M. Sena-Cruz, Pullout behaviour
509 of steel fibres in self-compacting concrete, *ASCE J. Mater. Civil Eng.*
510 22 (1) (2010) 1–9.
- 511 [12] S. Balakrishnan, D. W. Murray, Finite element prediction of reinforced
512 concrete behaviour, *Struct. Engrg. Rep. No. 138*, University of Alberta,
513 Canada (1986).
- 514 [13] T. Y. Chang, H. Taniguchi, W. F. Chen, Non-linear finite element anal-
515 ysis of reinforced concrete panels, *J. Struct. Eng.-ASCE* 113 (1) (1987)
516 122–140.

- 517 [14] A. Elwi, M. Hurdey, Finite element model for curved embedding rein-
518 forcement, *J. Eng. Mech.-ASCE* 115 (4) (1989) 740–757.
- 519 [15] P. Bhatt, M. S. Barj, G. F. Elnounu, M. Memon, Non-linear finite ele-
520 ment analysis of shearwall-floor slab junction, in: D. R. Owen, E. Hinton
521 (Eds.), *Second International Conference on Computational Plasticity*,
522 Swansea, Wales, 1989, pp. 1319–1330.
- 523 [16] A. Ranjbaran, Mathematical formulation of embedded reinforcements
524 in 3d bricks elements, *Communications in Numerical Methods in Engi-*
525 *neering* 12 (1996) 897–903.
- 526 [17] A. Van Hauwaert, J. G. M. Van Mier, Computational modelling of the
527 fibre-matrix bond in steel fibre reinforced concrete, in: H. Mihashi,
528 K. Rokugo (Eds.), *Fracture Mechanics of Concrete Structures*, Freiburg,
529 Germany, 1998, pp. 561–571.
- 530 [18] J. P. B. Leite, V. Slowik, H. Mihashi, Computer simulation of fracture
531 processes of concrete using mesolevel models of lattice structures, *Cem.*
532 *Concr. Res.* 34 (6) (2004) 1025–1033.
- 533 [19] J. E. Bolander, Numerical modelling of fibre reinforced cement com-
534 posites: linking material scales, in: M. Prisco, R. Felicetti, G. Plizzari
535 (Eds.), *6th RILEM Symposium on Fibre Reinforced Concretes*, Varenna,
536 Italy, 2004, pp. 45–60.
- 537 [20] F. Radtke, A. Simone, L. Sluys, A computational model for failure anal-
538 ysis of fibre reinforced concrete with discrete treatment of fibres, *Eng.*
539 *Fract. Mech.* 77 (4) (2010) 597–620.
- 540 [21] F. Radtke, A. Simone, L. Sluys, A partition of unity finite element
541 method for obtaining elastic properties of continua with embedded thin
542 fibres, *Int. J. Numer. Methods Eng.* 84 (6) (2010) 708–732.
- 543 [22] E. Gal, R. Kryvoruk, Meso-scale analysis of FRC using a two-step ho-
544 mogenization approach, *Comput. Struct.* 89 (11-12) (2011) 921–929.
- 545 [23] Z. Bazant, P. Gambarova, Rough cracks in reinforced concrete, *ASCE*
546 *J. Struct. Div.* 106 (4) (1980) 819–842.

- 547 [24] R. de Borst, P. Nauta, Non-orthogonal cracks in smeared finite element
548 model, *Eng. Comput.* 2 (1985) 35–46.
- 549 [25] J. G. Rots, Computational modelling of concrete fracture, Ph.D. thesis,
550 Delft University of Technology, Netherlands (1988).
- 551 [26] J. M. Sena-Cruz, Strengthening of concrete structures with near
552 surface mounted CFRP laminate strips, Ph.D. thesis, Dep.
553 Civil Engineering, Universidade do Minho, Portugal (2005)
554 (<http://hdl.handle.net/1822/11781>).
- 555 [27] A. Ventura-Gouveia, J. A. O. Barros, Álvaro Azevedo, J. Sena-Cruz,
556 Multi-fixed smeared 3D crack model to simulate the behaviour of fibre
557 reinforced concrete structures, in: T. Marques et al. (Eds.), CCC 2008 –
558 Challenges for Civil Construction, FEUP, Porto, 2008, pp. Paper T2–3,
559 11 pp.
- 560 [28] J. A. O. Barros, Comportamento do betão reforçado com fibras, análise
561 experimental e simulação numérica, Ph.D. thesis, Faculdade de Engen-
562 haria da Universidade do Porto, Portugal (in Portuguese) (1995).
- 563 [29] S. P. Shah, S. E. Swartz, C. Ouyang, Fracture mechanics of concrete
564 (application of fracture mechanics to concrete, rock and other quasi-
565 brittle materials), John Wiley & Sons, Inc., 1995.
- 566 [30] P. Z. Bazant, J. Planas, Fracture and size effect in concrete and other
567 quasibrittle materials, *New directions in Civil Engineering*, CRC Press,
568 Boca Raton, Florida, 1998.
- 569 [31] O. Zienkiewicz, R. Taylor, Finite element method – Vol. 1: The basis,
570 Butterworth-Heinemann, Oxford, England, 2000.
- 571 [32] H. A. W. Cornelissen, D. A. Hordijk, H. W. Reinhardt, Experimental de-
572 termination of crack softening characteristics of normal and lightweight
573 concrete, *HERON*, Fracture Mechanics and Structural Aspects of Con-
574 crete 31 (2) (1986) 45–56.
- 575 [33] P. Stroeven, J. Hu, Effectiveness near boundaries of fibre reinforcement
576 in concrete, *Mater. Struct.* 39 (2006) 1001–1013.

- 577 [34] S. P. Timoshenko, J. N. Goodier, Theory of Elasticity, McGraw-Hill,
578 New York, 1991.
- 579 [35] RILEM TC 162-TDF, Test and design methods for steel fibre rein-
580 forced concretes: Uni-axial tension test for steel fibre reinforced con-
581 crete, Mater. Struct. 34 (1) (2001) 3–6.
- 582 [36] RILEM TC 162-TDF, Test and design methods for steel fibre reinforced
583 concrete - bending test (final recommendation), Mater. Struct. 35 (253)
584 (2002) 579–582.
- 585 [37] CEB-FIP, CEB-FIP Model Code 1990: Design code, Ceb bulletin
586 d'information no. 190, CEB-FIP Comité Euro-International du Béton,
587 Paris, France (1993).

588 **6. List of Tables**

589 Table 1: Concrete properties used in the simulation.

590 Table 2: Tri-linear stress - strain diagrams used for modelling the fibres'
591 bond - slip behaviour.592 Table 3: Number of fibres and orientation factor at the crack surface of the
593 embedded fibre meshes used for obtaining the distinct numerical curves.

Table 1: Concrete properties used in the simulation.

Property	Series	
	Cf30	Cf45
Density	$\rho = 2.4 \times 10^{-5} \text{ N/mm}^3$	
Poisson's ratio	$\nu_c = 0.20$	
Young's modulus	41300 N/mm ²	40600 N/mm ²
Compressive strength	71.1 N/mm ²	67.2 N/mm ²
Tensile strength	4.6 N/mm ²	4.5 N/mm ²
Fracture energy	0.117 N/mm	0.114 N/mm
Crack band-width	$l_b = 5 \text{ mm}$ (equal to element height at the notch)	

Table 2: Tri-linear stress - strain diagrams used for modelling the fibres' bond - slip behaviour (see also Fig. 3)

α [deg]	θ [deg]	Series	Failure mode	$\sigma_{f,1}$ [MPa]	$\sigma_{f,2}$ [MPa]	$\sigma_{f,3}$ [MPa]	$\varepsilon_{f,1}$ [-]	$\varepsilon_{f,2}$ [-]	$\varepsilon_{f,3}$ [-]
0	[0-15[Cf30 & Cf45	Pullout	588	803	360	0.030	0.090	0.600
30	[15-45[Cf30	Rupture	453	679	905	0.016	0.050	0.200
		Cf45	Pullout	588	803	360	0.030	0.090	0.600
60	[45-75[Cf30 & Cf45	Rupture	283	362	656	0.020	0.160	0.400

Table 3: Number of fibres and orientation factor at the crack surface of the embedded fibre meshes used for obtaining the distinct numerical curves.

Test/Series	Tensile				Bending			
	Cf30		Cf45		Cf30		Cf45	
Numerical curve	A	B	A	B	A	B	A	B
Number of fibres	30	26	50	63	142	105	171	193
Orientation factor	0.687	0.701	0.658	0.662	0.780	0.765	0.773	0.761

594 **7. List of Figures**

595 Figure 1: Three-dimensional scheme of the crack plane: (a) stress compo-
596 nents, displacements and coordinate systems [27], (b) fracture modes.

597 Figure 2: Sketch of the intersection point P in the distinct domains.

598 Figure 3: Determination of the embedded fibre's stress - strain diagram based
599 on the experimental pullout force - slip relationship.

600 Figure 4: Three-dimensional scheme of the embedded fibre intersecting an
601 active crack (n is the vector normal to the crack plane).

602 Figure 5: Three-dimensional finite element mesh of the cylindric specimens:
603 (a) concrete phase, (b) fibre phase for the Cf30 series and (c) fibre phase for
604 the Cf45 series.

605 Figure 6: Numerical simulation of the uniaxial tensile tests for the Cf30
606 series (right hand graph is a close-up of the tensile-crack opening curve's
607 initial part).

608 Figure 7: Numerical simulation of the uniaxial tensile tests for the Cf45
609 series (right hand graph is a close-up of the tensile-crack opening curve's
610 initial part).

611 Figure 8: (a) and (b) Fibres at the crack surface, respectively, for the Cf30
612 and Cf45 series (light grey represents the specimen's notch and dark grey
613 squares are the fibres); (c) and (d) normal stresses for a $w=0.16$ mm, respec-
614 tively for the Cf30 and Cf45 series; (e) and (f) normal stresses for a $w=2$
615 mm, respectively for the Cf30 and Cf45 series.

616 Figure 9: Three-dimensional finite element mesh of the prismatic specimens:
617 (a) concrete phase and (b) fibres phase (Cf30 series).

618 Figure 10: Numerical simulation of the three-point bending tests for: (a)
619 Cf30 and (b) Cf45 series.

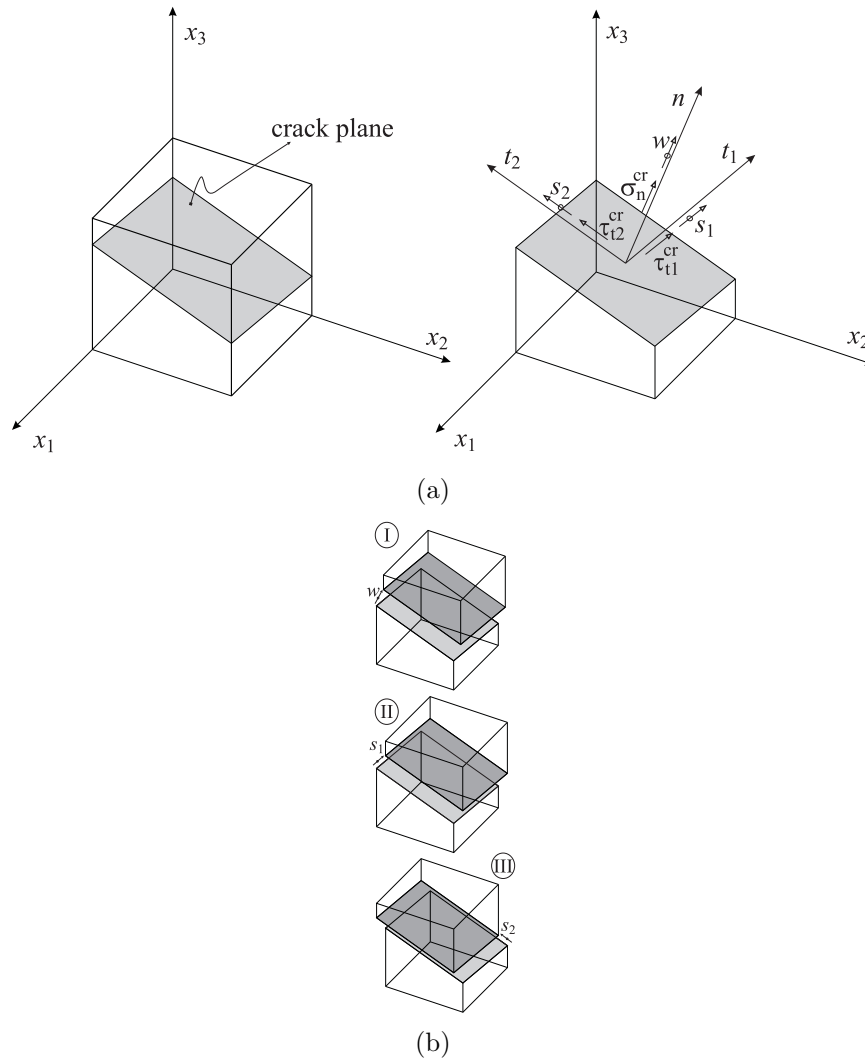


Figure 1: Three-dimensional scheme of the crack plane: (a) stress components, displacements and coordinate systems [27], (b) fracture modes.

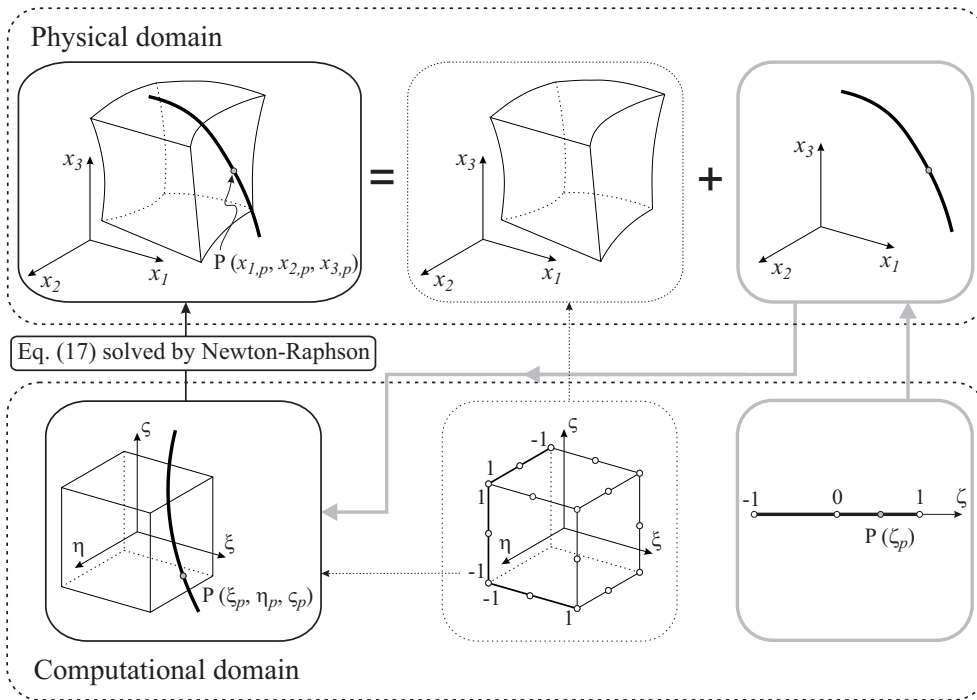


Figure 2: Sketch of the intersection point P in the distinct domains.

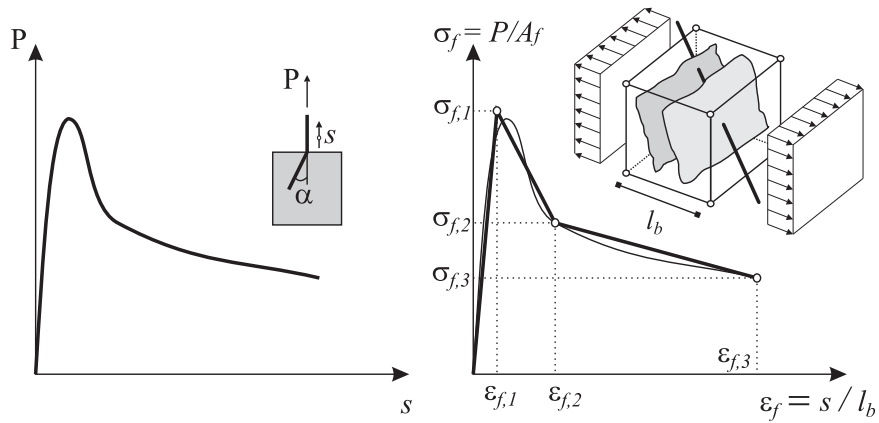


Figure 3: Determination of the embedded fibre's stress - strain diagram based on the experimental pullout force - slip relationship.

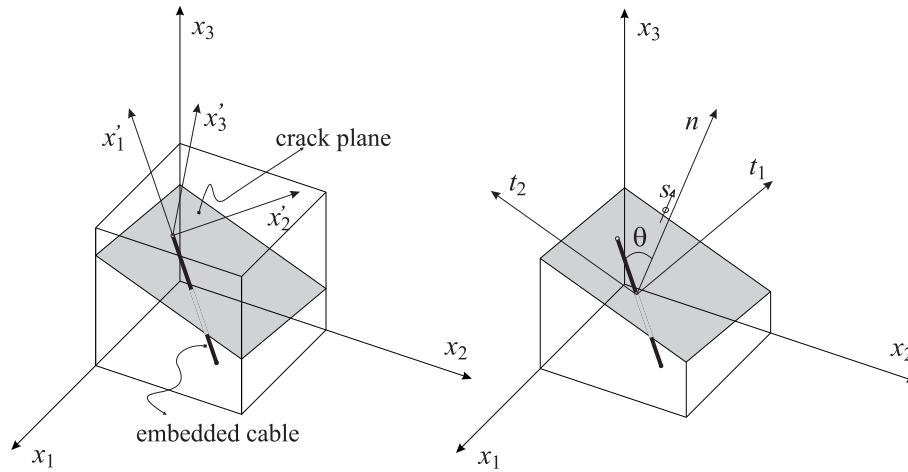


Figure 4: Three-dimensional scheme of the embedded fibre intersecting an active crack (\hat{n} is the vector normal to the crack plane).

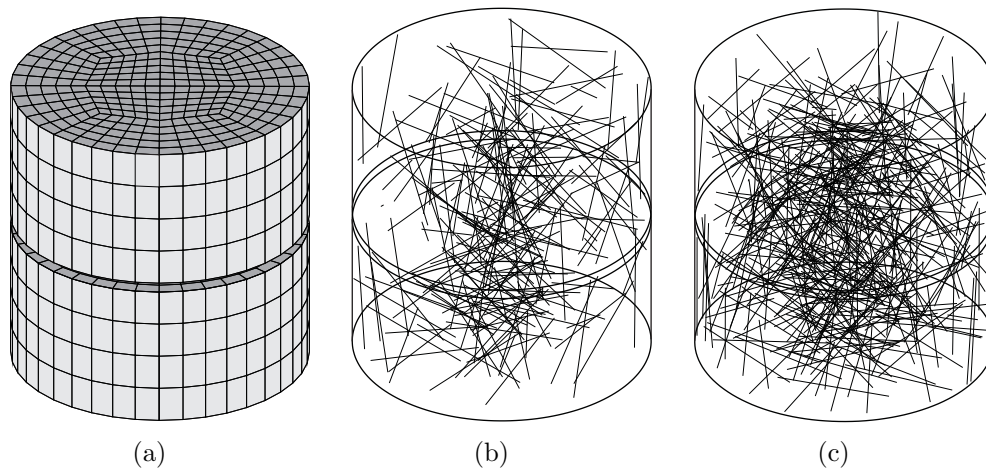


Figure 5: Three-dimensional finite element mesh of the cylindric specimens: (a) concrete phase, (b) fibre phase for the Cf30 series and (c) fibre phase for the Cf45 series.

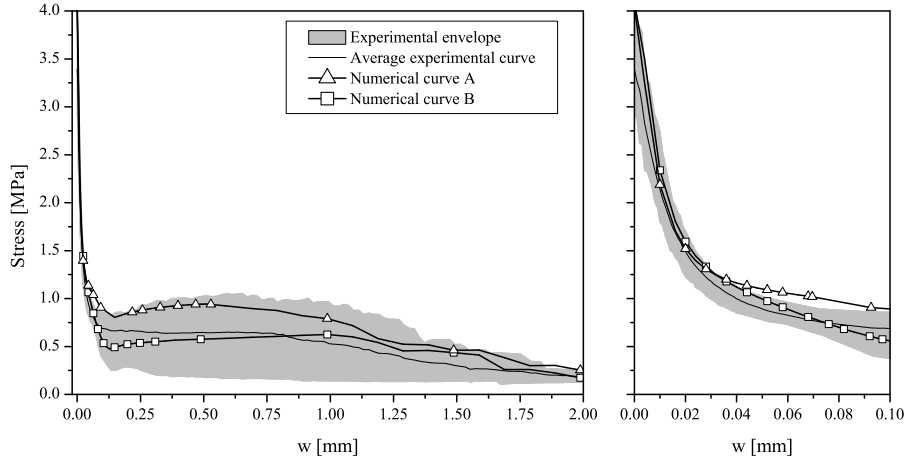


Figure 6: Numerical simulation of the uniaxial tensile tests for the Cf30 series (right hand graph is a close-up of the tensile-crack opening curve’s initial part).

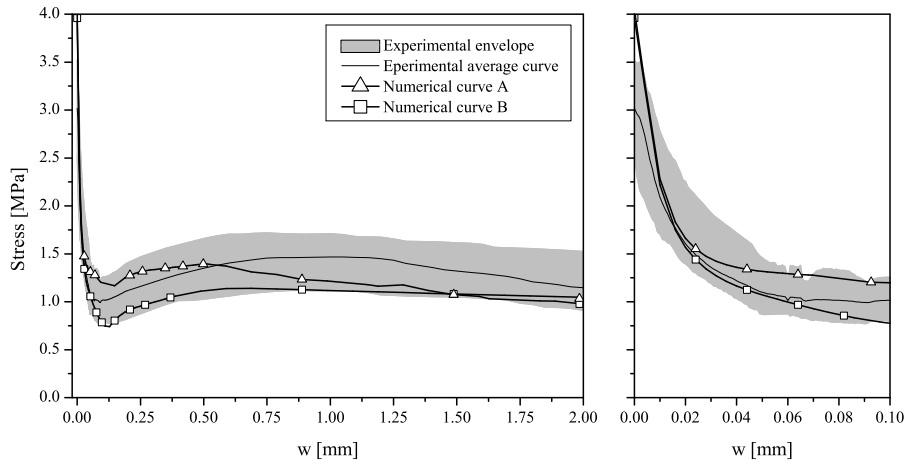


Figure 7: Numerical simulation of the uniaxial tensile tests for the Cf45 series (right hand graph is a close-up of the tensile-crack opening curve’s initial part).

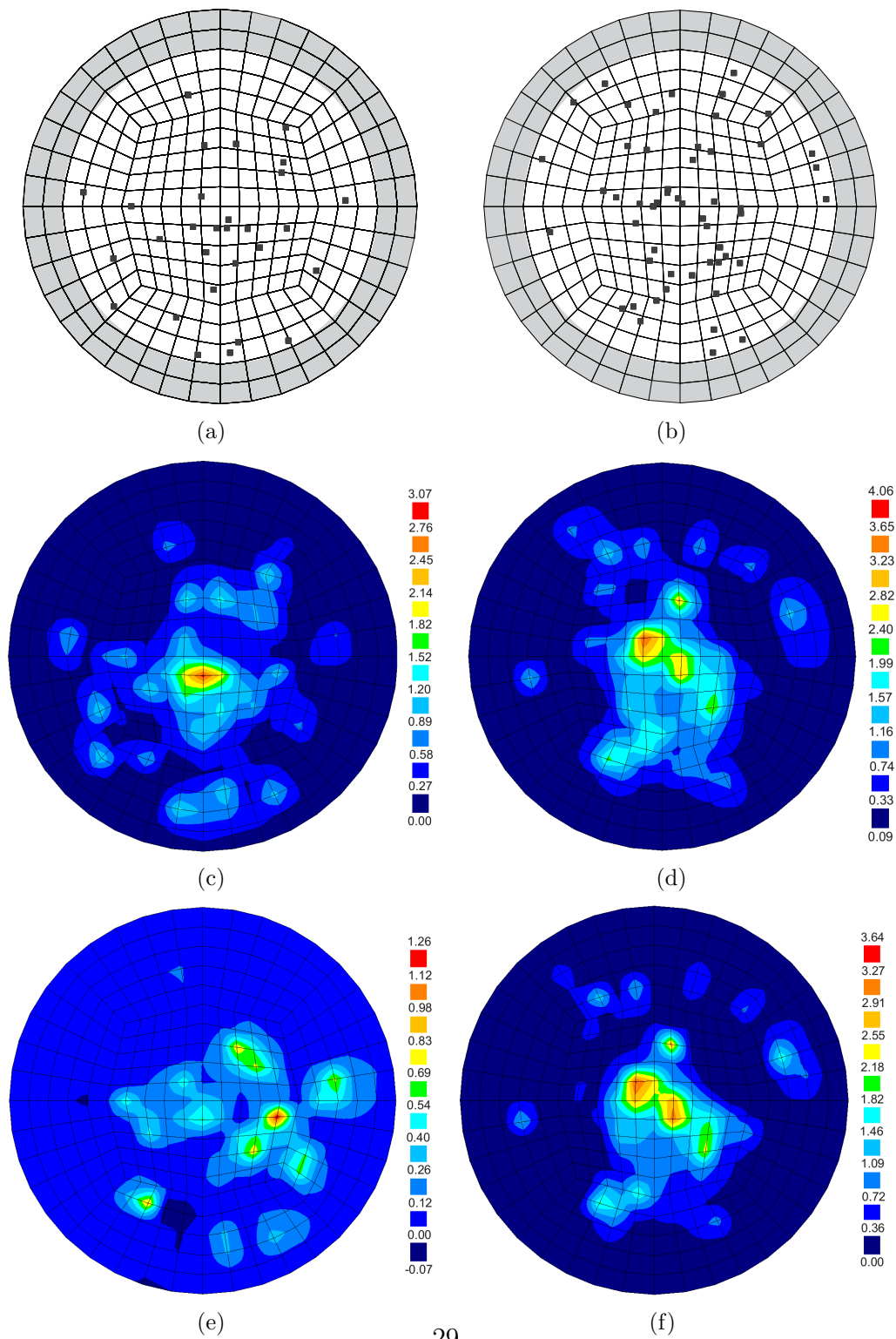
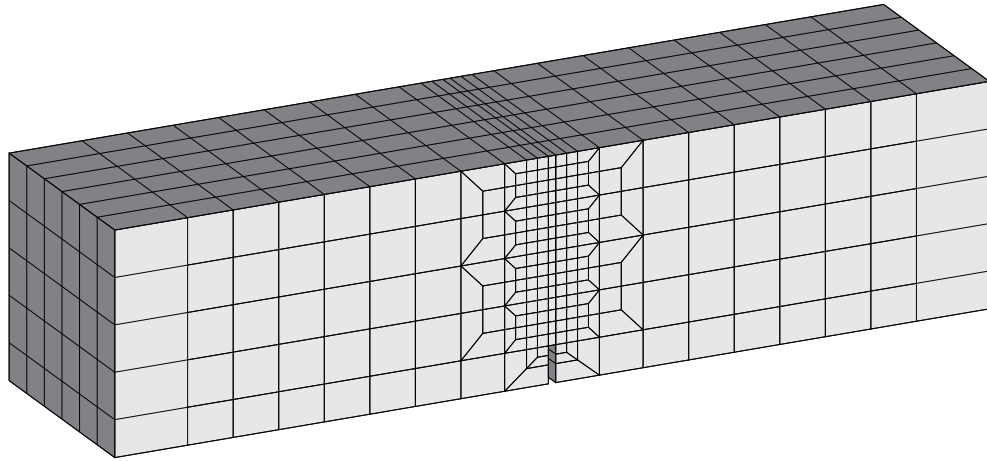
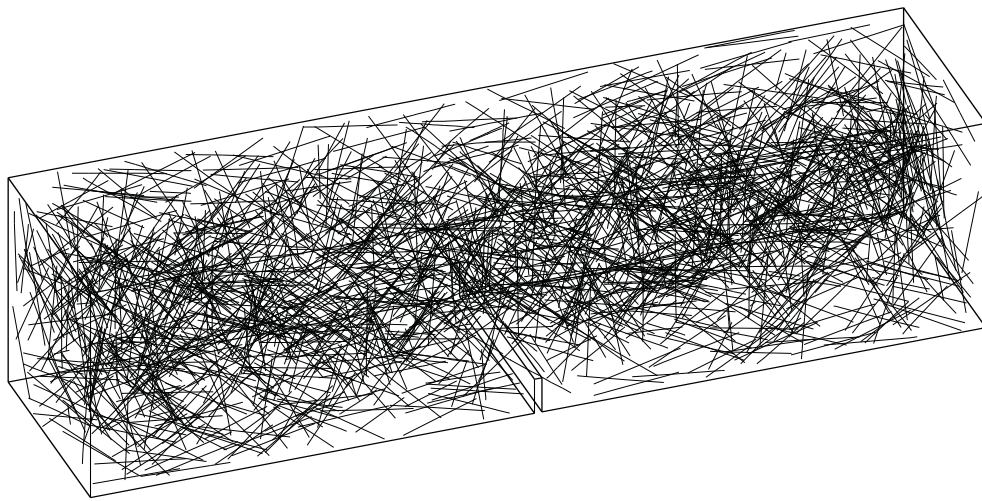


Figure 8: (a) and (b) Fibres at the crack surface for the Cf30 and Cf45 series, respectively (light grey represents the specimen's notch and dark grey squares are the fibres); (c) and (d) normal stresses for a $w=0.16$ mm for the Cf30 and Cf45 series, respectively; (e) and (f) normal stresses for a $w=2$ mm for the Cf30 and Cf45 series, respectively.



(a)



(b)

Figure 9: Three-dimensional finite element mesh of the prismatic specimens: (a) concrete phase and (b) fibres phase (Cf30 series).

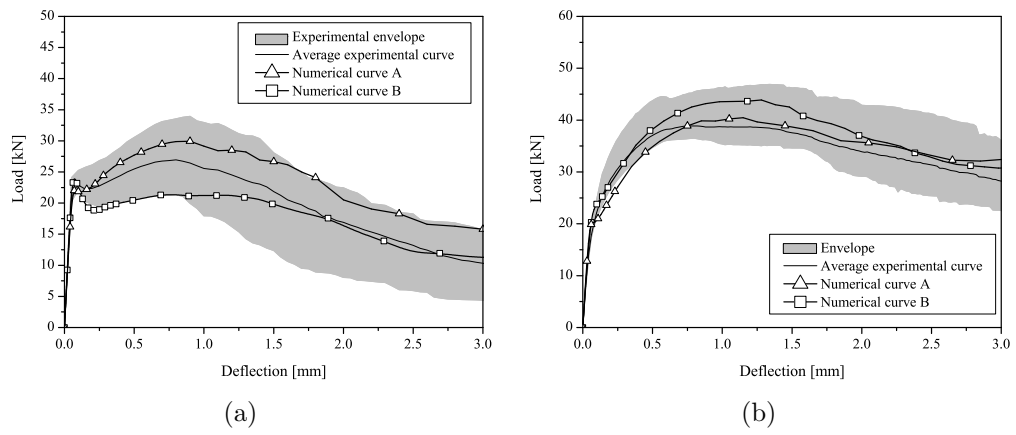


Figure 10: Numerical simulation of the three-point bending tests for: (a) Cf30 and (b) Cf45 series.

620 **Appendix A. Derivation of Eq. 10, after [26, 28]**

621 The constitutive matrix for the elasto-cracked concrete, D^{crco} , can be
622 obtained by the following procedure. Firstly, by incorporating Eqs. 2 and 5
623 into Eq. 7 yields,

$$\Delta \underline{\sigma} = \underline{D}^{co} \left(\Delta \underline{\varepsilon} - [\underline{T}^{cr}]^T \Delta \underline{\varepsilon}_l^{cr} \right) \quad (\text{A.1})$$

624 Pre-multiplying both members of Eq. A.1 by the crack strain transformation
625 matrix, \underline{T}^{cr} , leads to

$$\underline{T}^{cr} \Delta \underline{\sigma} = \underline{T}^{cr} \underline{D}^{co} \Delta \underline{\varepsilon} - \underline{T}^{cr} \underline{D}^{co} [\underline{T}^{cr}]^T \Delta \underline{\varepsilon}_l^{cr} \quad (\text{A.2})$$

626 On the other hand, the relationship between the incremental local crack
627 stress vector, $\Delta \underline{\sigma}_l^{cr}$, and the incremental stress vector in global coordinate
628 system, $\Delta \underline{\sigma}$, can be defined as:

$$\Delta \underline{\sigma}_l^{cr} = \underline{T}^{cr} \Delta \underline{\sigma} \quad (\text{A.3})$$

629 Substituting Eq. A.3 into the left member of Eq. A.2 renders,

$$\Delta \underline{\sigma}_l^{cr} + \underline{T}^{cr} \underline{D}^{co} [\underline{T}^{cr}]^T \Delta \underline{\varepsilon}_l^{cr} = \underline{T}^{cr} \underline{D}^{co} \Delta \underline{\varepsilon} \quad (\text{A.4})$$

630 The incremental crack strain vector in the local crack coordinate system is
631 obtained by including Eq. 8 into the left side of Eq. A.4,

$$\Delta \underline{\varepsilon}_l^{cr} = \left(\underline{D}^{cr} + \underline{T}^{cr} \underline{D}^{co} [\underline{T}^{cr}]^T \right)^{-1} \underline{T}^{cr} \underline{D}^{co} \Delta \underline{\varepsilon} \quad (\text{A.5})$$

632 At last, the constitutive law of the elasto-cracked concrete is obtained by
633 substituting Eq. A.5 in A.1, which yields:

$$\Delta \underline{\sigma} = \left(\underline{D}^{co} - \underline{D}^{co} [\underline{T}^{cr}]^T \left(\underline{D}^{cr} + \underline{T}^{cr} \underline{D}^{co} [\underline{T}^{cr}]^T \right)^{-1} \underline{T}^{cr} \underline{D}^{co} \right) \Delta \underline{\varepsilon} \quad (\text{A.6})$$

634 OR

$$\Delta \underline{\sigma} = \underline{D}^{crco} \Delta \underline{\varepsilon} \quad (\text{A.7})$$

635 where \underline{D}^{crco} , Eq. 10, is the constitutive matrix for the elasto-cracked concrete.